Quantum Efficiency Gain in 2D Perovskite Photo and X-Ray Detectors

Hsinhan Tsai, Lei Pan, Xinxin Li, Jinkyoung Yoo, Sergei Tretiak, Xuedan Ma, Lei R. Cao,* and Wanyi Nie*

The perovskite polycrystalline thin film detector fabricated by solution method is a promising low-cost, scalable technology for radiation imaging, but its thin volume limits the sensing efficiency for high-energy X-ray photons. This work reports 2D perovskite thin film photo-diodes with a detection gain when sensing visible and X-ray photons. Detailed power and temperature-dependent device characterizations reveal a charge multiplication effect to be responsible for the observed high gain. This is caused by a disparity in electron and hole transport, where electron transport is retarded by a trap/de-trap process via shallow trap states, whereas the hole transport is fast enough to produce a photoconductive gain in satisfying the charge neutrality. The 2D perovskite made with butylamine spacers is also found to exhibit a larger efficiency gain than those made with phenylethylamines because of the higher likelihood of forming shallow traps in the former. The thin film diodes feature a high temporal response over 1 MHz due to the fast charge collection across a thin volume, and the discovery provides device physics mechanisms in connection to material structure-function relationship for future optoelectronics design that can boost the efficiency of X-ray sensing and dim light detection.

1. Introduction

To fulfill the needs of large-scale X-ray imaging applications,[1,2] it is desirable to develop low-cost detectors that can be monolithically grown on the read-out chips. Perovskites semiconductor devices have shown great promise for detecting X-ray photons and other radiation signals featuring high sensitivities[3] and ultra-low detection limits.[4] 2-dimensional (2D) perovskite films can be built with high degree of crystallinity by wet chemistry methods with high dark resistivity yielding excellent photo-sensitivities. Our previous work has shown that the crystallinity and film uniformity of 2D thin film exceeds those of the 3-dimensional (3D) film, which are ideal candidate for upscaling X-ray digital panels. In the thin film structures, the intrinsic perovskite layer can be fully depleted by interfacing with selective contacts that further minimizes the dark noise.[1a]

H. Tsai, J. Yoo, S. Tretiak, W. Nie
Center for Integrated Nanotechnologies
Los Alamos National Laboratory
Los Alamos, NM 87545, USA
E-mail: wanyi@lanl.gov
H. Tsai
Department of Chemistry
University of California Berkeley
Berkeley, CA 94720, USA
L. Pan, L. R. Cao
Nuclear Engineering Program
Department of Mechanical and Aerospace Engineering
The Ohio State University

The ORCID identification number(s) for the author(s) of this article can be found under https://doi.org/10.1002/adom.202300847

© 2023 The Authors. Advanced Optical Materials published by Wiley-VCH GmbH. This is an open access article under the terms of the Creative Commons Attribution License, which permits use, distribution and reproduction in any medium, provided the original work is properly cited.

DOI: 10.1002/adom.202300847

L. Pan Department of Chemistry Northwestern University Evanston, IL 60208, USA X. Li, X. Ma Center for Nanoscale Materials Argonne National Laboratory Lemont, IL 60439, USA X. Li. X. Ma Consortium for Advanced Science and Engineering University of Chicago Chicago, IL 60637, USA S. Tretiak Theoretical Division Los Alamos National Laboratory Los Alamos, NM 87545, USA

Columbus, OH 43210, USA

E-mail: cao. 152@osu.edu





www.advopticalmat.de

Because the generated carriers are traveling across a shorter distance for signal generation in the thin film devices, a smaller bias or even zero bias is adequate to drive the detector to function. [1a,5] And charge carriers can be collected rapidly through a smaller volume which enables a fast detector response. Additionally, making a flexible digital panel for X-ray imaging using the thin film device structures is another appealing concept, [6] which bring values and open-up the desires for developing a wearable dosimeter, [6a] lightweight panels [7] and 3D imaging applications.

However, there are critical shortcomings when using thin film devices for high-energy photon sensing. The thin film typically has a significantly smaller thickness than single crystals (e.g., um vs mm in thickness) that results in a limited absorption of the high-energy X-rays. The incomplete X-ray absorption leads to a low intrinsic detection efficiency and hence a low X-ray sensitivity. For instance, a typical methylammonum lead triiodide [8] single crystal device can deliver a high sensitivity of $10^6~\mu C~Gy_{air}^{-1}~cm^{-2}$ whereas the thin film devices typically output a moderate sensitivity of $10-1000 \,\mu\text{C Gy}_{air}^{-1} \,\text{cm}^{-2}$, more than 1000 times lower than that of a single crystal device. One simple approach to increase the sensitivity is to further increased the thin film thickness, but uniformly upscaling the thickness by solution method is not straightforward. To contrive a thick layer, a highly concentrated precursor is utilized which increases the number of nucleation seeds during the coating process. Consequently, a large number of crystallites will form in the layer, creating more defects as recombination centers that undermine desirable properties (e.g., mobility (μ) and lifetime (τ)) for charge carrier transport.

Another approach to improve the sensitivity is to achieve a higher quantum efficiency gain (also known as photoconductive gain) that has been observed in organic detectors, [9] perovskite single crystal X-ray detectors, [1a,2,10] and photodetectors. [11] In this work, we report an X-ray detection gain in 2D perovskite thin film diodes driven by charge multiplication induced by hole injection at high electric fields. Our detector shows 20 to 400 times higher sensitivities than the calculated sensitivity without a gain, resembling the highest sensitivity among the reported thin film detectors. We further analyzed the noise and detection limit for the devices. Because of the high charge density collected in the gain regime, the signal-to-noise ratio (SNR) remains above 30. To obtain a SNR of 10, the lowest detectable limit of our detector with gain is 2.13 $\mu Gy_{\rm air}~s^{-1}.$ The high gain is confirmed by a >1000%External Quantum Efficiency (EQE) from the same device tested under visible light. Detailed device characteristics and carrier mobility measurements are performed, where we attribute the gain effect to an ambipolar carrier transport lifetime that drives an excessive hole injection from the electrode. The ambipolar transport lifetime originates from a significantly delayed electron transport by trap states, which are validated by time-resolved photocurrent and photoluminescence measurements. Interestingly, the choice of the organic spacer plays a key role in the observed multiplication gain effect. 2D perovskites with butylamine show a much-enhanced gain than that with phenylethylamine cations. Exfoliated single-crystal devices are also fabricated where crystals with more conducting edges exhibit a stronger efficiency gain. These results point to that the defects created by the organic cation vacancies in the 2D perovskite film and crystals contribute to these shallow trap states. The butylamine molecule has a lower

boiling point and can easily leave more vacancies that produces more shallow traps. Finally, we demonstrate that our device has a fast temporal response, with a frequency bandwidth of 1 MHz. This gain mechanism can be used to enhance the thin film device's detection sensitivity to high-energy X-rays source. Our investigation also shed light on future material engineer in controlling the organic species in the 2D perovskite structure for further enhance the multiplication gain and detector sensitivity.

2. Results and Discussion

The device architecture employed in this work is sketched in Figure 1a. Briefly, we started with a transparent conducting substrate (indium tin oxide, ITO) that was coated with a 40 nm layer of poly[bis(4-phenyl) (2,4,6-trimethylphenyl)amine as the p-type charge collection interface. A thick 2D perovskite layer with 7 – 10 µm thick was then coated on the PTAA employing a previously developed method, [1b] yielding a compact crystalline film. The 2D perovskite has a chemical formula of BA2MA2Pb3I10 $(BA^{+} = butylamine (CH₃(CH₂)₃NH₂⁺), MA⁺ = methylamine$ (CH₃NH₂+)). The film was characterized by X-ray scattering, scanning electron microscopy, and optical spectroscopy which are presented in Figures S1-S4 (Supporting Information). The RP phase structures are confirmed by X-ray scattering pattern in Figure S4 (Supporting Information). A 60 nm of fullerene layer, a 10 nm of bathocuproine layer, and 50 nm of gold were thermally evaporated on the perovskite layer serving as *n*-type charge collection layers and the top electrode. Finally, a layer of Al₂O₃ is evaporated on top of the metal for protection purposes.

We first tested the devices' sensitivity under X-ray irradiations with an X-ray beam generated by a silver anode with a characteristic peak energy of 22.1 keV (maximum 50 keV). By fitting the linear regression of the X-ray-induced current (charge density) against the dose rate curves in Figures S5-S7 (Supporting Information), the detection sensitivities as a function of the applied electric field can be extracted. Figure 1b shows typical responses of a 10 μm device when the X-ray beam is turned on and off with increasing dose rate, driving under two electrical fields. Figure 1c shows the extracted sensitivity as a function of electrical fields. As shown in Figure 1c, both devices started with low sensitivities of 24 and 130 μ C Gy_{air} $^{-1}$ cm $^{-2}$ at zero fields. When the field increases to 0.5 V μm^{-1} , the sensitivities of both devices first quickly increase and tend to stabilize \approx 485 and 3700 μ C Gy_{air} $^{-1}$ cm $^{-2}$. At higher fields, the sensitivities continue to rise at a faster rate to 1031 and 21 995 μC Gy_{air} $^{-1}$ cm $^{-2}$ respectively. A similar rapid sensitivity rise at higher fields is also observed when the device is exposed to a high-energy tungsten source shown in Figure S7 (Supporting Information). Based on the film thickness and material's optical bandgap, we estimated a sensitivity without a gain for our device. The detailed estimation method is described in Supporting Information. For a thickness of 5 – 10 µm perovskite devices, we obtained a sensitivity in the range of 23–46 μ C Gy_{air} ⁻¹ cm⁻², which is close to the measured sensitivity at zero bias. The higher measured sensitivities are also likely from the contribution of the low energy X-ray absorption, or film thickness variation. The probed high sensitivities at high fields greatly exceed the calculated sensitivity indicating a possible photoconductivity gain.

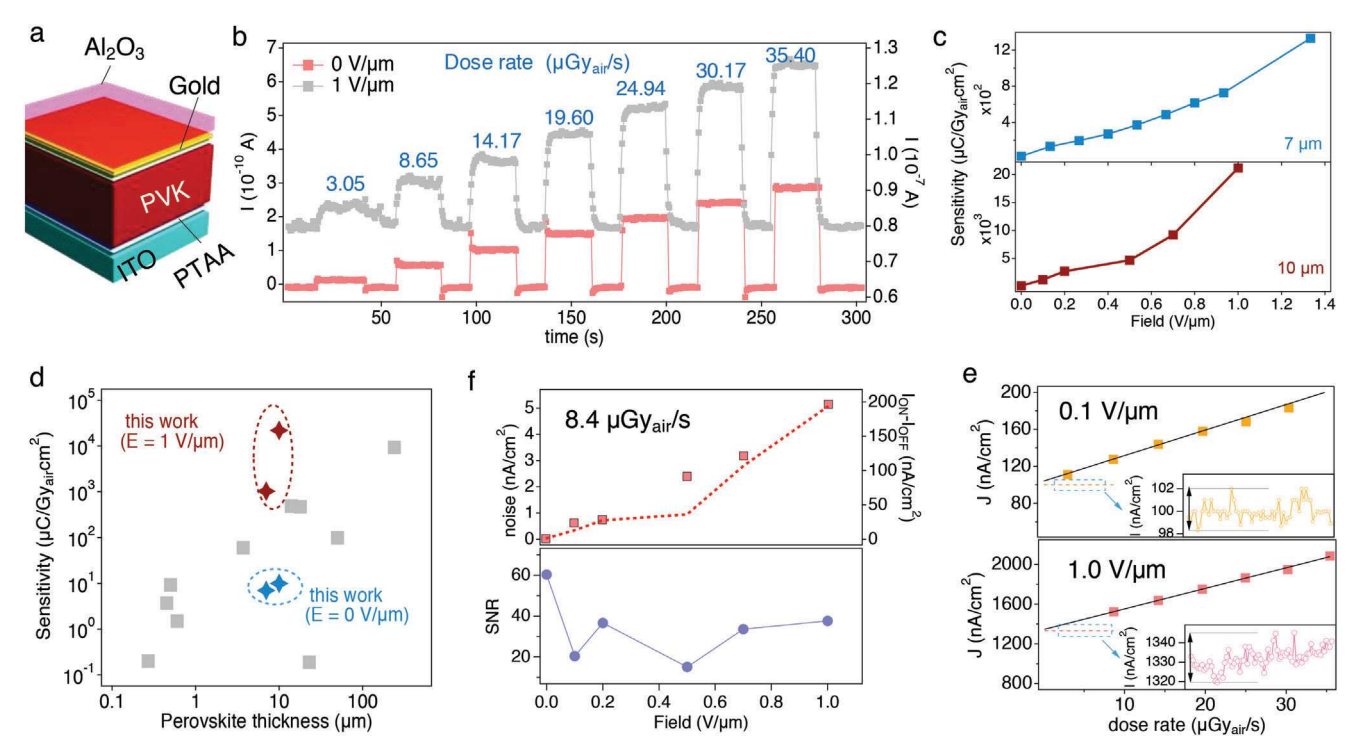


Figure 1. X-ray detector performances. a) The schematic of the planer *p-i-n* device architecture investigated in this study. b) Typical time evolution of the photocurrent response from our thin film detector when the X-ray beam was turned on and off with increasing dose rate. c) Extracted sensitivity as a function of applied electrical fields showing the photocurrent gain when the device was exposed under 22.1 keV (maximum 50 keV) X-ray beam. d) X-ray detection sensitivities of thin film devices plotted as a function of perovskite layer thickness. Gray symbols are the reported values from the literature, and colored symbols are from our work. f) (upper) standard deviation of the noise against applied electrical field plot and the X-ray induced signal by subtracting the dark current from the photo-signal. (lower) The SNR estimated from the top plot as a function of applied electrical field. e) Photocurrent signal as a function of X-ray dose rate for two applied fields.

To compare the performance of our device to those reported in the literature, $^{[1a,5b,6a-e,10c,12]}$ we summarized the reported sensitivity values as a function of film thickness in Figure 1d. As a variety of X-ray energies are employed which drastically impact the resulting sensitivities, here we choose the devices tested under X-ray energies between 8 and 30 keV for this comparison. And the sensitivities were taken when the devices were driven under no or low fields (< 0.3 V μm^{-1}). Clear, the sensitivity values scale with the film thickness benefitted from the better X-ray attenuation. The sensitivities of our detectors tested under zero field also fit in this trend. However, our detectors output 1–2 orders of magnitude higher sensitivities compared to those with similar thicknesses that deviate from the observed trend at the high field (1 V μm^{-1}). The significantly higher sensitivity values at higher electrical fields are thus from the photo-conductivity gain.

After validating the photo-conduction gain effect, next we investigate another two metrics, namely the SNR and the detection limit. The noises are estimated from the standard deviation of the baseline fluctuation, which are plotted with the X-ray induced signals in Figure 1f as a function of applied electrical fields. Figure 1f top panel shows that the detection signal ($I_{\rm ON}\text{-}I_{\rm OFF}$) increases with higher electrical fields, and is accompanied with higher noises. This is attributed to high fields level up dark baselines that inevitably introduce more dark noises. Because of the noises, the SNR drops from 60 at 0 V μm^{-1} to \approx 15 at 0.5 V μm^{-1} in the lower panel in Figure 1f. However, because the X-ray induced signal

was substantially higher at higher fields with gains, the SNR rises back to above 30. To estimate the low detection limit, we plot the linear dependence of the X-ray current and extrapolate the cut-off current by its dark baseline as illustrated in Figure 1e. Here, to obtain a SNR of 10, we estimate the lowest detectable photocurrent from our device. And use the photocurrent as the input to the linear fit in Figure 1e, the lowest detectable dose rate can be extrapolated. With this method, we obtain a detection limit of 1.04 and 2.13 $\mu Gy_{air}/s$ for 0.1 V/ and 1.0 V μm^{-1} respectively.

To confirm the gain effect, we next quantify the device's EQEs and probe their field- and power-dependent responses with a precalibrated light-emitting diodes (LEDs). Additionally, Figure 2 compares another 2D perovskite made with phenylethylamine (PEA) as the organic spacer. The reason for choosing PEA as a comparison is because of its higher boiling point (195 °C) that is more heat tolerant during the processing. Figure 2a,b presents the dark current (I)- electrical field (E) characteristics for the BA and PEA devices under forward and reverse scans. The forward turn-on fields for both diodes are at $\approx + 0.2 \text{ V} \mu\text{m}^{-1}$, but the forward injection current amplitude of the PEA device is 50 times lower than that of the BA device. A lower forward injection suggests the absorber is more insulating which can be attributed to a few factors, like more structural disorder, less trap, or poor carrier mobility. In the reverse bias regime, both devices exhibit comparably low dark current near zero bias, indicating both devices have similar Schottky contact energy barrier that

www.advancedsciencenews.com

www.advopticalmat.de

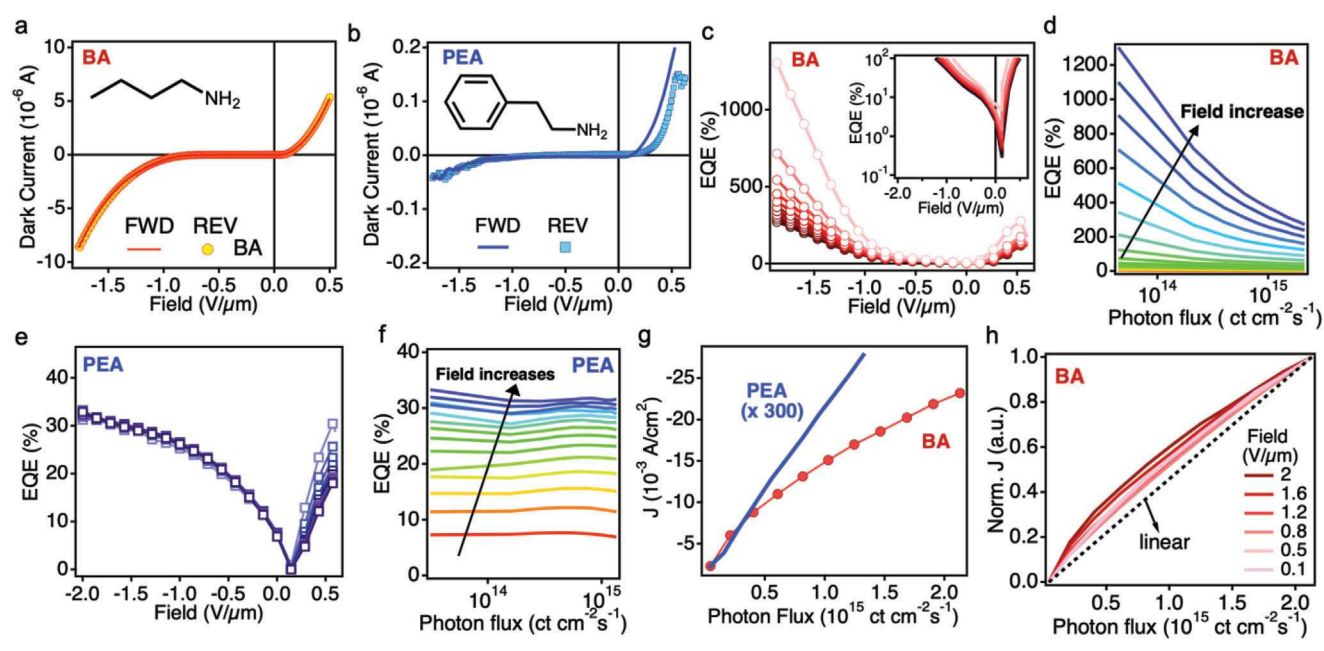


Figure 2. Device characterized with a calibrated blue LED. Dark current as a function of electrical field for devices made with a) BA, and b) PEA 2D perovskites. Solid lines are curves scanned from forward to reverse bias (FWD) and symbols are scanned from reverse to forward bias (REV). EQE for c) BA device and e) PEA device plotted against electrical field. The colors changing from light to dark correspond to a varying photon flux from low to high. Similarly, EQEs are plotted against the photon flux for d) BA device, and f) PEA device. g) A plot overlaps the power-dependent photocurrent curves of the two devices. And h) the normalized photocurrent of the BA device as a function of photon flux. Different colors correspond to the applied reverse fields. The dashed line is a linear curve to guide the eye.

limits charge injection from the electrode. Once the field exceeds $-0.7 \text{ V} \,\mu\text{m}^{-1}$, a significant dark current jump from the BA device was observed, whereas that of the PEA device remains relatively low. The dark current jump is due to Schottky contact breakdown as validated later in this work by temperature-dependent currentvoltage measurements. We notice that in the forward bias regime, the PEA device's *I–E* curves have hysteresis. This is likely because the sweep was taken from forward bias to reverse bias direction which triggers the mobile ion movements. To minimize the slow transient response from field-driven ion migrations, instead of sweeping I-E curves, we acquire the time evolution of the device's current at each bias while turning the blue LEDs on and off and as shown in Figure S8 (Supporting Information), from which the stabilized dark and photocurrent at each bias are extracted. The stabilized dark I-E curve (Figure S8b, Supporting Information) can replicate the dark I-E curves shown in Figure 2a,e,g., dark current remains flat at low fields followed by a rapid jump at a high field when the Schottky contact breakdown occurs. Subtracting the stabilized photocurrent by the corresponding dark current yields the extracted photo carriers, which enables evaluation of the EQE.

Figure 2c–f presents the devices' power and field-dependent EQEs. In Figure 2c, the BA device's EQE is less than 1% without an external field because the internal field across a thick layer ($\approx\!8~\mu m$) is too weak to drift all the carriers, and the charge collection relies on carrier diffusion. When the electric field increases, the EQE quickly rises and reaches a saturation at $\approx\!25\%$ when the applied reverse field is $\approx\!0.7~V~\mu m^{-1}$. When continuing to apply higher fields up to 1.9 V μm^{-1} , the BA device's EQE drastically increases to 500% at a high photon flux and to 1500% at

a low photon flux. This behavior duplicates the X-ray sensitivity behavior shown in Figure 1, where a gain effect is observed after the Schottky contact breakdown. Figure 2d displays the BA device's EQE against incident photon flux curves, and a strong photon flux dependence is observed, i.e., lower photon flux, higher EQE. We further studied the EQE of the BA devices with a thinner 2D perovskite layer (Figure S9, Supporting Information), the amplification and power-dependent behaviors persist in this device, suggesting the device characteristics are independent of the thickness of the film.

Figure 2e,f presents the EQEs of the PEA device as a comparison. Without the electrical field, the PEA device also has a low EQE of $\approx\!0.5\%$ due to the high recombination loss through the thick film. The EQE of the PEA device rises accordingly with increase the electrical field, but it slows down at 0.5 V μm^{-1} and saturates at $\approx\!30\%$. In contrast to the BA device's EQE gains, the PEA device's saturation still holds at higher fields (1–2 V μm^{-1}). The power dependence of the PEA device's EQE also differs from that of the BA device. As shown in Figure 2f, its EQEs weakly depend on the incident photon flux under all reverse electrical fields.

To visualize the difference between the two devices, Figure 2g overlays the photocurrent density of BA and PEA devices as a function of photon flux collected under an electrical field of $1~V~\mu m^{-1}$. The PEA device has a linear photocurrent-photon flux dependence, whereas the BA device deviates from a linear relationship at higher photon fluxes. Such a deviation in BA device is attributed to a space charge accumulation that hinders the ideal charge collection efficiency across the device when the charge density is high. Figure 2h also shows a normalized photocurrent

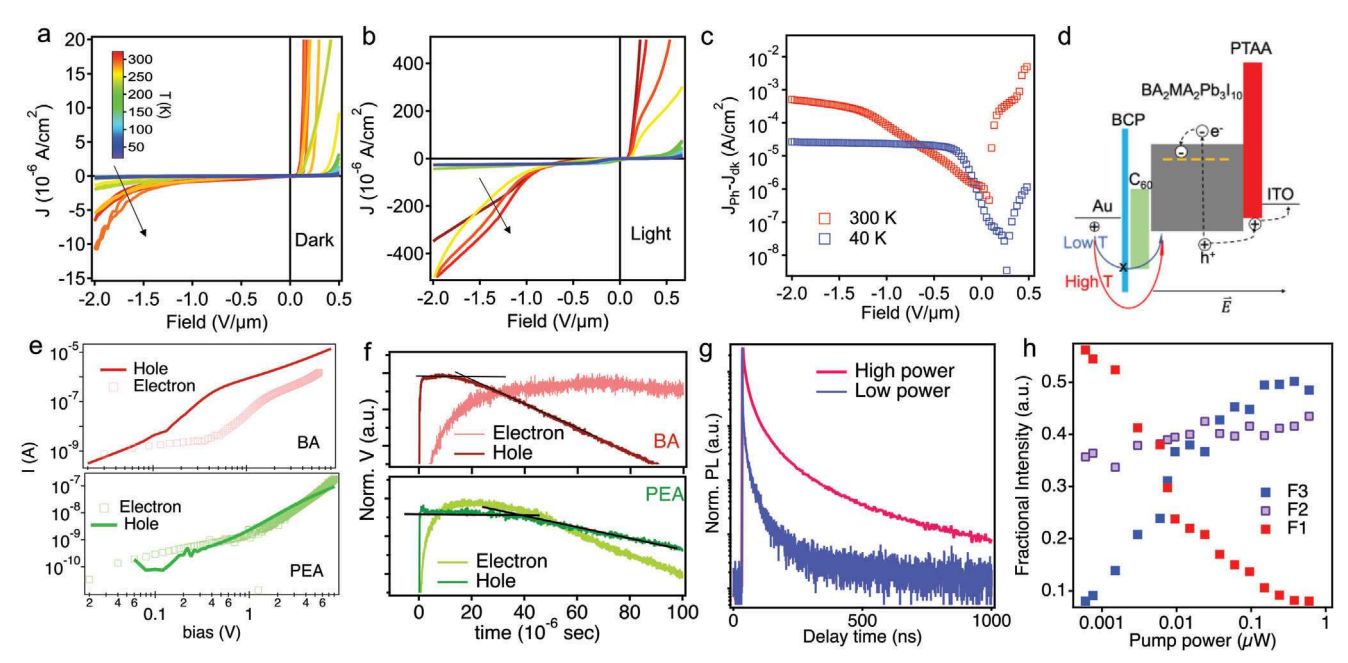


Figure 3. Carrier transport and recombination properties. a) Dark and b) photo J–E curves measured under various temperatures. c) Extracted photocurrent (J_{ph} – J_{dark}) as a function of applied electrical field when measured under 300 K versus 40 K. d) Schematic diagram illustrating the hole injection effect at low and high temperatures in this device. e) Space charge limited electron and hole current as a function of applied voltage for BA devices and PEA devices. Here solid lines are hole current and square symbols correspond to electron current. f) Time of flight photocurrent decay curves comparing electron and hole drifts for BA and PEA devices. g) PL decay curves for BA thin films at two different powers; and h) extracted fractions of the short and long lifetime components for BA thin film as a function of excitation power.

of the BA device to compare the sub-linear behavior under different applied fields. Interestingly, the sub-linear behavior gets more pronounced at higher fields. This is because a large charge injection occurs at high reverse fields after the Schottky contact breakdown in the BA device that effectively increases the space charge density.

From this analysis, we conclude that the high electrical field drives an EQE gain in the BA device, whereas the gain effect is negligible in the PEA device at high fields. Accompanied with the gain, the BA device's photocurrent shows a strong light power dependence, the gain effect is enhanced at lower photon flux. In sharp contrast, the PEA device does not show the power dependence and its EQEs remain almost unchanged for all photon fluxes.

To further understand the electronic mechanism for the observed photo-sensitivity gain, we performed temperaturedependent photo and dark current density (I)-E characterizations as shown in Figure 3a-c extracts the difference of dark and photocurrent under two temperatures (300 K vs 40 K) as a function of field. Markedly, both the reverse bias breakdown current and forward bias dark current drop sharply with the reduced temperature. The photocurrent plotted in Figure 3b exhibits a similar trend, where the high reverse field photocurrent rapidly drops and the slope near the high field *J–E* curves also becomes flatter. Figure 3c compares the device's current density difference $\Delta J = J_{\rm ph} - J_{\rm dark}$ as a function of field for the device measured at 300 K versus that measured at 40 K. Unlike the room temperature measurements, Δ I first increases with reverse field and then saturates at higher fields in low temperature (40 K). This is in concurrence with the dark current trend

where the reverse dark current can be suppressed during temperature decrease. The fact that the reverse dark current breakdown is a thermally activated process suggests that the current injection from the metal electrode into perovskite is thermionic emission that dominated Schottky contact breakdown, instead of tunneling breakdown or avalanche because both are temperature independent. This process is illustrated in Figure 3d and the surface's work functions are confirmed by Ultraviolet photoelectron spectroscopy measurements presented in Figure S10 (Supporting Information). At room temperature, Schottky barrier lowering at higher reverse voltage leads to the injection of the opposite charge species that promotes recombination (Figure S11, Supporting Information). When the temperature is decreased, the electrons have less thermal energy to overcome the Schottky barrier between the metal electrode and perovskite, which results in higher reverse breakdown voltage and smaller forward dark current. The Schottky contact breakdown turns the originally blocking Schottky contact into a non-blocking Ohmic contact that allows charge injection.

The photoconductive gain is described by:^[13]

$$Gain = \frac{carrier\ recombination\ lifetime}{transient\ time} \tag{1}$$

A high gain can be obtained when the minority carrier recombination lifetime is longer than the transient time, which allows for the photo-generated carrier to accumulate in the semiconductor leading to an effective charge multiplication.^[13] Such a lifetime difference originates from an ambipolar carrier transport where one type of carrier is significantly slower and not



www.advopticalmat.de

available for recombination, while another type of carrier travels much faster and can be injected from the electrode to maintain the charge neutrality. An ambipolar carrier transient can be obtained via various mechanisms, such as intrinsic traps, [9a] interface junction, [14] nano-structures [15] etc. One possible mechanism that is responsible for the gain observed in our system is the presence of shallow traps that capture one type of carriers, leading to ambipolar charge transport.

To gain deeper insights into the type of the traps in BA devices, we then investigate the carrier transport and recombination lifetime of the BA and PEA devices. Figure 3e plots the space charge limited (SCL) current-voltage characteristics of electron only and hole only devices assemble with BA and PEA films. Interestingly, a large discrepancy between the electron and hole currents of the BA device is observed, whereas the SCL currents overlap reasonably well in the PEA device case. This is the first indication of the ambipolar charge transport in BA device due to electron traps. Additionally, the photocarrier mobility is probed by timeof-flight (ToF) experiment, the setup is described in the method section. Briefly, a pulsed laser generates a flux of electron-hole pairs near one interface and one type of carriers are drifted to the counter electrode that produces a current pulse. Depending on the polarity of the applied field on the counter electrode, either electron or hole is drifted. The detailed decay curve analysis is presented in Figure S12 (Supporting Information), and different laser powers were checked to ensure the carrier concentration is sufficiently low and does not perturbate the applied electrical fields during the experiment. Figure 3f plots the ToF photocurrent decay curves for the BA device and PEA device. The decay curves for hole current in both devices display a transition point near 10 µs (BA) and 30 µs (PEA). This transition shifts to an earlier time with higher fields as shown in Figure S13c (Supporting Information). The hole mobility for BA device is estimated to be 0.08 V cm⁻² s whereas that of the PEA device is slightly lower at 0.03 V cm⁻² s. The slightly reduced mobility in the PEA device can be attributed to the crystalline structure disorder in the film revealed by scanning electron microscopy and X-ray scattering patterns shown in Fig. S1 and Fig. S3, supporting information. In stark contrast, the electron transient curve for the BA device extends toward a much longer time scale where a slow rise is observed and extended beyond 100 µs. This slow rise is typically attributed to the charge trapping effect, [16] where electron transport is via a trap/de-trap process through shallow trap states in case of BA device. The electron transient curve for PEA device also exhibits a similar slow rise indicating that electron de-trapping also exists in the PEA device, but it decays at a much earlier time point than that of the BA device. These data suggest that the hole transport in both devices is not severely affected by traps, and the discrepancy between the electron and hole transport in BA device is much more prominent.

To future probe the carrier recombination process in the BA thin films, we measure the carrier recombination lifetimes via time-resolved photoluminescence (TRPL) spectroscopy at various laser powers. The results are summarized in Figure 3g,h. Figure 3g compares the TRPL curves of a BA thin film when excited at a high laser power and a low laser power. Interestingly, we find that the PL decay is shortened when lower power is employed whereas higher excitation power yields a longer lifetime. To rationalize the pump power-dependent PL decay behavior, we

fit the TRPL curves with three exponential functions (described in Figure S13 Supporting Information) and extract the three lifetime components (τ_1 , τ_2 , and τ_3), with their percentage ratios (F_1 , F_2 , F_3) defined as,

$$F_i = \frac{A_i \tau_i}{A_1 \tau_1 + A_2 \tau_2 + A_3 \tau_3}, \quad i = 1, 2, 3$$
 (2)

The data are plotted in Figure 3h as a function of the excitation power. The three-component model fits our data better than the two-component model shown in Figure S13 (Supporting Information). The pump power-dependent F_i values suggest percentage changes in the number of photons exhibiting the different lifetimes, hence indicative of the associated recombination processes. Although slight variations in the lifetime values can be observed as the pump power increased, the slow component (F_1) is on the order of ≈ 1 µs and remains significantly longer than the other two components, which are determined to be ≈ 0.1 ns (F_2) and 0.01 ns (F_3) , respectively. Most notably, the percentage ratio of the slow component (F₁) plumbed from more than 50% at low powers to only ≈10% at high powers, in stark contrast to the two fast components which raise with power. Similar phenomena were observed in various samples and locations (see Figure S14, Supporting Information). Based on these observations, we speculate that the slow component has dominate contributions from trap-assisted recombination processes:[17] upon increasing the excitation power and hence the initial carrier densities, the trap states are filled up, leading to a suppression of the long lifetime component at high powers. A detailed analysis by Pean et al^[18] revealed a complex recombination path that includes bimolecular-trap-de-trap that defines the TRPL kinetics. Three rate constants can be obtained from this model that are in concurrence with our analysis. These TRPL dynamics measurements further confirmed the critical role of trap states played in the carrier lifetimes and likely associated with their transport properties.

Briefly, we found out that shallow electron trap states exist in the BA device, which supports that the trap-assisted photoconductive gain effect is the mechanism for the high sensitivity in X-ray and photo-detectors. Specifically, we found the hole mobility is much higher than the electron mobility by SCL and ToF measurements. And from the photocurrent decay profile of electron, its lifetime is retained for a much longer time. The extended electron lifetime is attributed to a trap/de-trap process via shallow trap states. The optical spectroscopy characterizations further suggest the existence of electron trap states. The presence of the trap states is further confirmed by the higher trap density in the electron current in the SCL curves in Figure S15 (Supporting Information). Therefore, the electron traps states contribute to the imbalance of electron and hole transport, which leads to high photoconductive gain.

After validating the gain mechanism, the molecular origin of the electron trap states is still elusive at this stage. We hypothesize that shallow traps are created by material defects tied to the vacancies sites during the thin film processing. The EQE dependence on the photon flux of the BA device (Figure 2d) agrees with the so-called dynamic-range enhancing gain compression due to carriers filling in the shallow traps .^[19] We also recognize that the performance of the polycrystalline thin film devices can be

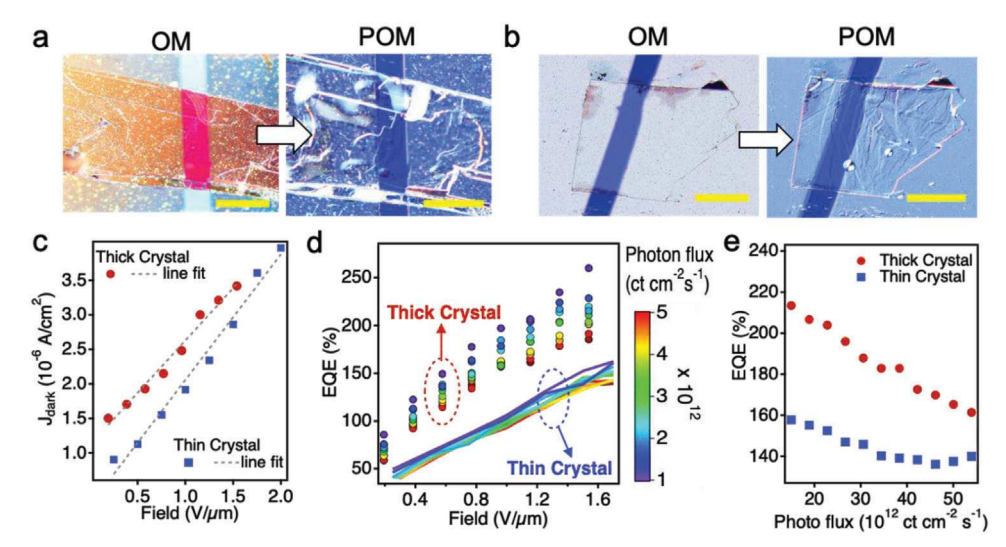


Figure 4. Exfoliated single crystal device performances. Optical microscopy image with and without polarizer for a) a thick crystal and b) a thin crystal. The scale bars in a-b are $100 \mu m$. c) Dark current as a function of electrical fields. d) EQE against field plot for both devices illuminated under various LEDs powers. e) EQEs of both devices as a function of photon flux under $1 \text{ V} \mu m^{-1}$ electrical field.

affected by many factors, such as grain boundary, surface, phase impurity. To obtain insights into the intrinsic properties, we fabricated devices on exfoliated 2D perovskite crystals and anticipate that exfoliating the crystals to thinner layers can remove the edges in the device's channel which can suppress the formation of shallow trap states. The device structure and the resulting EQEs are summarized in **Figure 4**.

The devices' morphologies are first visualized by optical microscopy (OM) and polarized optical microscopy (POM). As the thicker crystal shown in Figure 4a, it has more crystal edges and boundaries that are present in the conducting channel, which is much more obvious in the POM images. Once the crystals are exfoliated to a thinner thickness, the number of edges is reduced in the channel, yielding a much cleaner surface as shown in Figure 4b. The devices are characterized in the same way as the film devices where the time evolution of the photo and dark currents are collected to quantify the EQE (Figure S16, Supporting Information). Unlike the polycrystalline devices, the single crystal devices show a flat dark baseline without current drifting even at higher fields, suggesting the ion migration effect is smaller in the single crystals (Figure S16, Supporting Information).

The dark current density (A cm⁻²) as a function of the applied field is extracted by the time evolution curves and are plotted in Figure 4c. The dark current density is higher in the thicker device than that of the thin crystal device under the same field because there are more conducting channels within the thick polycrystalline crystal due to a poor Schottky contact quality and more defects. Figure 4d compares the EQE-*E* field curves of the thick crystal and the thin crystal devices when illuminated with various photon fluxes. As the result, both devices show EQEs exceeding 100% at higher fields. Notably, the thin crystal device shows a moderate gain whereas the thick crystal device exhibits a more pronounced gain. Accompanied with the higher gain, the thick crystal device has a more obvious power dependence with a higher EQE when illuminated with a low light power. In contrast, the power-dependent EQE curves of the thin crystal device

merge together. This is reflected in Figure 4e, where the power-dependent EQEs are plotted together when the devices are both under 1 V μm^{-1} field. Clearly, the thicker crystal device has a steeper power-dependent EQE curve than that of the thin crystal device. These results indicate that the gain effect along with the power dependence can be suppressed in the thin crystal device where fewer conducting edges are present in the channel. And in the thick device case, more conducting edges exist which enhance the gain effect.

Under a high gain regime assisted by the long charge recombination time, one concern could be the slow temporal response. Therefore, we further demonstrate that our photo-diode can respond at a high speed because of the fast hole transport time in **Figure 5.** Figure 5a shows the device's rise and decay curves after a short 1 ns laser pulse when the device is driven under different electrical fields. The device's rise time (τ_R) and decay time (τ_D) are defined by the time duration when the photocurrent rises from 10% to 90%, and decays from 90% to 10%. At low field, the device rises within 0.07 µs and decays within 0.9 µs. Both raise and decay times are shortened when higher E fields are applied by field enhanced carrier drifting. Figure 5b shows the photocurrent response to varying input laser's frequency. At low frequencies (1 to 10 kHz), the photocurrent remains flat with negligible loss in the output current. The cut-off frequency when the device losses 50% of the initial current occurs above 1 MHz. In low field regime, the cut-off frequency increases from 2.2 to 2.9 MHz, because of a more efficient carrier drifting with fields that shorten the decay time. Above the gain regime when the field is higher than $1.2 \text{ V} \,\mu\text{m}^{-1}$, the cut-off frequency slightly drops back to 2.3 MHz.

3. Discussion

To briefly summarize the experimental observations from the device and material characterizations, we observe an imbalanced transport lifetime between electron and hole, causing a charge multiplication that facilitates the detection gain. The gain effect

ADVANCED OPTICAL MATERIALS

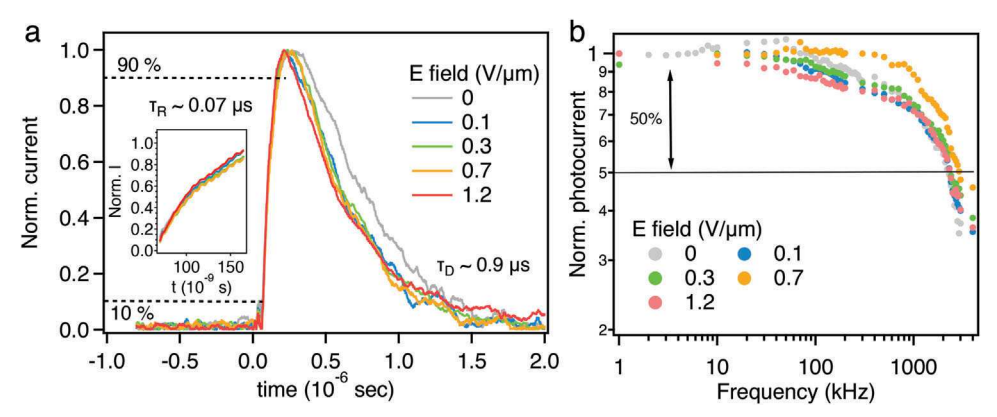


Figure 5. Temporal response of the 2D perovskite photo-diode. a) Time response of the photocurrent normalized by its maximum point after a laser pulse. b) Photocurrent normalized with the low frequency photo-current as a function of laser frequency. Different colors represent different electrical folds.

is drastically suppressed once the temperature is lowered due to reduced charge injection across the Schottky barrier. The extended electron transport lifetime with electron trap and de-trap process indicates that the electron traps are shallow states located below the conduction band. We also notice that the gain is always accompanied by a light intensity dependence, e.g., the gain is enhanced at lower photon flux. This is because higher photon fluxes tend to fill up the shallow trap which eliminates the electron trapping effect. The observed gain and power dependence in the 2D perovskites depends on the choice of the organics, i.e., device made with BA spacer has a larger gain and one with PEA spacer has a negligible gain. More organics have experimented and the device characteristics are shown in Figure S17 (Supporting Information). Based on these results, we hypothesize that 2D perovskites made with BA have a higher likelihood of forming shallow traps, and the traps are created by BA vacancy because BA has a low boiling point and escapes more easily. The BA escaping mechanism is also recently observed in the single crystals which contribute to the conducting edge states.^[20] This is in concurrence with our single crystal device results, where device made with a thick crystal with more conducting edges has a higher quantum efficiency gain at high fields.

After probing the mechanism, here we provide speculations on several possible molecular origins. Our previous publication has revealed an unusually long carrier diffusion length in the $BA_2MA_2Pb_3I_{10}$ 2D Ruddlesden-Popper (RP) phase single crystal device.^[21] We have attributed such an extended diffusion length to the trapping and de-trapping process by shallow trap states in the system. Beside, the first principles simulations of BA₂PbI₄ 2D-RP perovskite materials further explored in detail the effects of a variety of defects (such as BA, iodine and Pb/I vacancies and iodine interstitials) on the electronic structure .[22] These defects have low-formation energies and are common given the typical iodine redox chemistry in both 3D and 2D-RP systems. Computational results confirm the robust electronic structure of the material where the benign defects such as BA or BA+I or Pb+I2 vacancies barely perturb the electronic bands. In particular, BA vacancies lead to the formation of the shallow electronic trap sites, which is likely the case for devices studied in the present contribution. In contrast, defect chemistries related to the iodine may result in I-vacancies or I-interstitials, significantly

perturb the valance band with a characteristic formation of deep trap states .^[23]

In addition, our recent work has probed an usually long carrier diffusion length in higher n numbered RP perovskite single crystals, and attributed it to the shallow trap states present in the 2D perovskites.^[21] These results echo with several other reports where the shallow trap states are found responsible for the extended carrier diffusion.^[24] The molecular origin of the shallow trap states in the BA system is still unknown. The higher trap density is usually tied to the degree of crystallinity of the material or surface defects. In Figure S3 (Supporting Information), we compared the crystallinity of the two films and found that the crystallinity of BA thin film is better than that of the PEA. On the other hand, we performed UPS characterizations for both films and found the work function of the BA is slightly deeper than that of the PEA thin film. This indicates a moderate p-type doping near the surface. This could be a possible origin for the observed shallow traps. While the molecular origins worth deeper material characterizations, our finding in this current work along with the trap assisted long carrier diffusions reveal the important role of the shallow trap states in 2D perovskite systems, leading to a beneficial effect on the opto-electronic devices.

4. Conclusion

We revealed the mechanism of shallow electron trap-assisted photoconductive gain effect of a 2D BA perovskite device, which can be used to enhance the quantum efficiency in perovskite photo and X-ray detectors. In the BA device, thermionic emission dominated Schottky contact breakdown at higher reverse electric field and higher temperature which allow charge injection, and the imbalance of electron and hole transport due to electron traps that leads to a high photoconductive gain for the BA device. While the prerequisites for a radiation detector capable of gamma spectroscopy are the large volume single crystal with as less interfaces and traps as possible, [24a,25] the electron or hole traps that existed in thin film devices for X-ray detection might not be necessarily as a negative factor, as discussed in this paper. Our results also point out the important role of controlling the shallow defects in the 2D perovskite system and their benign effect on the opto-electronic properties.



www.advopticalmat.de

5. Experimental Section

Thin Film and Device Fabrication: 2D perovskite precursor was first prepared by dissolving Pbl₂ (99.999% trace metal basis), Methylammonium iodide (MAI), n-Butylammonium iodide (BAI) (or Phenethylammonium iodide, PEAI) in anhydrous N,N-Dimethylformamide (DMF) in an Ar filled glovebox. The molar ratio of Pbl₂:MAI:BAI (or PEAI) was kept at 3:2:2. The Pb²⁺ concentration in DMF was kept at 3 m. The precursor was first heated at 120 °C for 1 h to fully dissolve the materials in DMF.

The pre-cleaned indium tin oxide substrates were treated by oxygen plasma and then a stoke solution of poly[bis(4-phenyl) (2,4,6-trimethylphenyl) amine in chlorobenzene (20 mg ml $^{-1}$) was spin coated on the substrate. The coated substrates were annealed in the Ar filled glovebox at 150 °C for 1 h and then were heated at 165 °C for 5 min. Next the substrates were quickly transferred to a spin coater chunk and the hot perovskite precursor was quickly dropped on the substrate, the spin coater was immediately started to spin the substrate at 3000 rpm without ramping. Thirty seconds after the spin coating started, the substrates were taken for post annealing at 65 °C for 20 h to ensure any residual solvents were removed.

X-ray Detector Characterization: The X-ray detection performances were quantified by exposing the devices under various X-ray beams and collect their dark and X-ray induced responses. The difference between the dark and photo responses were used to calculate the charge density induced by X-ray.

The 8.1 keV X-ray was generated from a Rigaku Ultima III diffractometer that used a fine line sealed X-ray tube with Cu-K α target operated at 40 kV with 50 μ A tube current. The dose rate was calibrated by a Radical, 10×6 -6 μ 0 ion chamber, and the dose rate was reduced by placing aluminum thin foils between the beam and the device.

X-ray (22.1 keV, maximum 50 keV0) was produced by an Ag anode tube (Amptek Mini-X X-ray tube), the X-ray tube was operated at voltage higher than 22.2 kV, and the does rate was tuned by changing the tube current. The X-ray dose rate was calibrated by a Fluke Biomedical RaySafe 452 dosimeter.

X-ray (80 keV) was generated by a tungsten anode tube. The tube was operated under various voltages at 100 and 140 kV, and the dose rate was calibrated by a Radical, 10×6 -6 M ion chamber at each voltage and tube current. After calibration, the device was placed at the same place with the ion chamber for sensitivity measurements.

Device External Quantum Efficiency Characterizations: The power of a blue LED was first measured by a calibrated silicon photo-diode (Thorlabs, FDS100) when the silicon diode was placed in front of the LED at a distance of 5 cm. After the calibration, the devices were placed at the same place with the silicon diode, in front of the LED. The devices were driven at constant reverse biases, while the LED was turned on and off. The current from the devices were constantly acquired by a LabView program, and the photocurrent was extracted subtracting the square wave of the light induced current by the stabilized dark baseline.

Time of Flight Mobility Measurements: The device was mounted according to the experimental setup illustrated in Figure S10 (Supporting Information). A bias was applied on the ITO of the device, and the voltage signal was collected by an oscilloscope from a resistor (1 kohm) connected in series with the device. A 435 nm pulsed laser was utilized to generate a flux of electron/hole pairs at the perovskite/ITO interface. Since the perovskite materials were direct gap materials, the penetration depth of the blue photon was much smaller than the thickness (\approx 7 μ m). A positive voltage was applied for hole transient curve measurement, and the voltage was negative when measuring electron current.

Time Resolved Photoluminescence: The pump power dependent, time-resolved PL decay curves were measured using a home-built confocal laser microscope. A 400 nm pulsed diode laser was used to excite the samples. PL signals from the samples were collected using a microscope objective and directed to single photon avalanche diodes. The excitation power was adjusted by adding various neutral density filters to the excitation path.

Supporting Information

Supporting Information is available from the Wiley Online Library or from the author.

Acknowledgements

The authors acknowledge Mr. Matthew Sheats from Los Alamos National Laboratory (LANL) for providing access to the X-ray beam and helping with acquiring the X-ray detector's responsivity data. W.N. acknowledges the mission foundation research project support by the Laboratory Directed Research Directions program office (LDRD) at LANL. W.N. and S.T. acknowledge the funding support of the exploratory research project by LDRD office at LANL. H.T. acknowledges the financial support from the J. Robert Oppenheimer (JRO) Distinguished Postdoc Fellowship at LANL. This work was performed, in part, at the Center for Integrated Nanotechnologies, an Office of Science User Facility operated for the U.S. Department of Energy (DOE) Office of Science by LANL (Contract 89233218CNA000001). X.L. acknowledges support from the National Science Foundation DMR Program under the award no. DMR-1905990. Work performed at the Center for Nanoscale Materials, a U.S. Department of Energy Office of Science User Facility, was supported by the U.S. DOE, Office of Basic Energy Sciences, under Contract No. DE-AC02-06CH11357. This research used resources (beamline 8-ID-E) of the Advanced Photon Source, a U.S. Department of Energy (DOE) Office of Science User Facility, operated for the DOE Office of Science by Argonne National Laboratory under Contract DE-AC02-06CH11357. This research used resources (beamline 7.3.3) of the Advanced Light Source, a U.S. DOE Office of Science User Facility under contract no. DE-AC02-05CH11231. R.C and L.P. acknowledge the support by the U.S. Department of the Defense, Defense Threat Reduction Agency under Grant HDTRA1-19-1-0024.

Conflict of Interest

The authors declare no conflict of interest.

Data Availability Statement

The data that support the findings of this study are available in the supplementary material of this article.

Keywords

2D perovskites, charge multiplication, quantum efficiency, X-ray detector

Received: April 23, 2023 Revised: June 1, 2023 Published online:

- [1] a) Y. Lei, Y. Li, C. Lu, Q. Yan, Y. Wu, F. Babbe, H. Gong, S. Zhang, J. Zhou, R. Wang, R. Zhang, Y. Chen, H. Tsai, Y. Gu, H. Hu, Y.-H. Lo, W. Nie, T. Lee, J. Luo, K. Yang, K.-I. Jang, S. Xu, *Nature* 2022, 608, 317;
 b) H. Tsai, S. Shrestha, L. Pan, H.-H. Huang, J. Strzalka, D. Williams, L. Wang, L. R. Cao, W. Nie, Adv. Mater. 2022, 34, 2106498.
- [2] Y. C. Kim, K. H. Kim, D.-Y. Son, D.-N. Jeong, J.-Y. Seo, Y. S. Choi, I. T. Han, S. Y. Lee, N.-G. Park, *Nature* 2017, 550, 87.
- [3] a) B. Xiao, Q. Sun, F. Wang, S. Wang, B.-B. Zhang, J. Wang, W. Jie, P. Sellin, Y. Xu, J. Mater. Chem. A 2021, 9, 13209; b) H. Li, J. Song, W. Pan, D. Xu, W.-a. Zhu, H. Wei, B. Yang, Adv. Mater. 2020, 32, 2003790.



www.advopticalmat.de

- [4] R. Zhuang, X. Wang, W. Ma, Y. Wu, X. Chen, L. Tang, H. Zhu, J. Liu, L. Wu, W. Zhou, X. Liu, Y. Yang, Nat. Photonics 2019, 13, 602.
- [5] a) P.-T. Lai, H.-C. Lin, Y.-T. Chuang, C.-Y. Chen, W.-K. Cheng, G.-H. Tan, B.-W. Hsu, L. Yang, S.-C. Lou, L.-J. Chien, H.-W. Wang, H.-W. Lin, ACS Appl. Mater. Interfaces 2022, 14, 19795; b) Z. Gou, S. Huanglong, W. Ke, H. Sun, H. Tian, X. Gao, X. Zhu, D. Yang, P. Wangyang, Phys. Status Solidi Rapid Res. Lett. 2019, 13, 1900094.
- [6] a) S. Demchyshyn, M. Verdi, L. Basiricò, A. Ciavatti, B. Hailegnaw, D. Cavalcoli, M. C. Scharber, N. S. Sariciftci, M. Kaltenbrunner, B. Fraboni, Adv. Sci. 2020, 7, 2002586; b) L. Basiricò, S. P. Senanayak, A. Ciavatti, M. Abdi-Jalebi, B. Fraboni, H. Sirringhaus, Adv. Funct. Mater. 2019, 29, 1902346; c) J. Liu, B. Shabbir, C. Wang, T. Wan, Q. Ou, P. Yu, A. Tadich, X. Jiao, D. Chu, D. Qi, D. Li, R. Kan, Y. Huang, Y. Dong, J. Jasieniak, Y. Zhang, Q. Bao, Adv. Mater. 2019, 31, 1901644; d) A. Ciavatti, R. Sorrentino, L. Basiricò, B. Passarella, M. Caironi, A. Petrozza, B. Fraboni, Adv. Funct. Mater. 2021, 31, 2009072; e) H. Mescher, F. Schackmar, H. Eggers, T. Abzieher, M. Zuber, E. Hamann, T. Baumbach, B. S. Richards, G. Hernandez-Sosa, U. W. Paetzold, U. Lemmer, ACS Appl. Mater. Interfaces 2020, 12, 15774; f) J. Guo, Y. Xu, W. Yang, B. Xiao, Q. Sun, X. Zhang, B. Zhang, M. Zhu, W. Jie, ACS Appl. Mater. Interfaces 2021, 13, 23928.
- [7] T. Zou, C. Chen, B. Xiang, Y. Wang, C. Liu, S. Zhang, H. Zhou, presented at 2019 IEEE International Electron Devices Meeting (IEDM), San Francisco, CA, USA, December 2019.
- [8] L. Pan, S. Shrestha, N. Taylor, W. Nie, L. R. Cao, Nat. Commun. 2021, 12, 5258
- [9] a) L. Li, F. Zhang, W. Wang, Q. An, J. Wang, Q. Sun, M. Zhang, ACS Appl. Mater. Interfaces 2015, 7, 5890; b) L. Basiricò, A. Ciavatti, T. Cramer, P. Cosseddu, A. Bonfiglio, B. Fraboni, Nat. Commun. 2016, 7, 13063; c) A. Ciavatti, T. Cramer, M. Carroli, L. Basiricò, R. Fuhrer, D. M. De Leeuw, B. Fraboni, Appl. Phys. Lett. 2017, 111, 183301.
- [10] a) J. Zhao, L. Zhao, Y. Deng, X. Xiao, Z. Ni, S. Xu, J. Huang, Nat. Photonics 2020, 14, 612; b) W. Pan, H. Wu, J. Luo, Z. Deng, C. Ge, C. Chen, X. Jiang, W.-J. Yin, G. Niu, L. Zhu, L. Yin, Y. Zhou, Q. Xie, X. Ke, M. Sui, J. Tang, Nat. Photonics 2017, 11, 726; c) S. Yakunin, M. Sytnyk, D. Kriegner, S. Shrestha, M. Richter, G. J. Matt, H. Azimi, C. J. Brabec, J. Stangl, M. V. Kovalenko, W. Heiss, Nat. Photonics 2015, 9, 444.
- [11] a) J. Feng, C. Gong, H. Gao, W. Wen, Y. Gong, X. Jiang, B. Zhang, Y. Wu, Y. Wu, H. Fu, L. Jiang, X. Zhang, Nat. Electron. 2018, 1, 404; b)

- M. I. Saidaminov, V. Adinolfi, R. Comin, A. L. Abdelhady, W. Peng, I. Dursun, M. Yuan, S. Hoogland, E. H. Sargent, O. M. Bakr, *Nat. Commun.* **2015**, *6*, 8724; c) L. Dou, Y. Yang, J. You, Z. Hong, W.-H. Chang, G. Li, Y. Yang, *Nat. Commun.* **2014**, *5*, 5404.
- [12] a) S. Deumel, A. van Breemen, G. Gelinck, B. Peeters, J. Maas, R. Verbeek, S. Shanmugam, H. Akkerman, E. Meulenkamp, J. E. Huerdler, M. Acharya, M. García-Batlle, O. Almora, A. Guerrero, G. Garcia-Belmonte, W. Heiss, O. Schmidt, S. F. Tedde, *Nat. Electron.* 2021, 4, 681; b) J. Peng, K. Ye, Y. Xu, L. Cui, R. Li, H. Peng, Q. Lin, *Sens. Actuator A Phys.* 2020, 312, 112132.
- [13] J. Kim, M. Kang, S. Lee, C. So, D. S. Chung, Adv. Mater. 2021, 33, 2104689.
- [14] a) W. Wang, F. Zhang, M. Du, L. Li, M. Zhang, K. Wang, Y. Wang, B. Hu, Y. Fang, J. Huang, *Nano Lett.* **2017**, *17*, 1995; b) X. Zhou, D. Yang, D. Ma, A. Vadim, T. Ahamad, S. M. Alshehri, *Adv. Funct. Mater.* **2016**, *26*, 6619.
- [15] H.-Y. Chen, M. K. F. Lo, G. Yang, H. G. Monbouquette, Y. Yang, Nat. Nanotechnol. 2008, 3, 543.
- [16] A. Musiienko, J. Pipek, P. Praus, M. Brynza, E. Belas, B. Dryzhakov, M.-H. Du, M. Ahmadi, R. Grill, Sci. Adv. 2020, 6, eabb6393.
- [17] S. D. Stranks, V. M. Burlakov, T. Leijtens, J. M. Ball, A. Goriely, H. J. Snaith, Phys. Rev. Appl. 2014, 2, 034007.
- [18] E. V. Péan, S. Dimitrov, C. S. De Castro, M. L. Davies, Phys. Chem. Chem. Phys. 2020, 22, 28345.
- [19] J. He, K. Qiao, L. Gao, H. Song, L. Hu, S. Jiang, J. Zhong, J. Tang, ACS Photonics 2014, 1, 936
- [20] Y. Miao, Z. Xiao, Z. Zheng, D. Lyu, Q. Liu, J. Wu, Y. Wu, X. Wen, L. Shui, X. Hu, K. Wang, Z. Tang, X.-F. Jiang, Adv. Sci. 2022, 9, 2201046.
- [21] S. Shrestha, X. Li, H. Tsai, C.-H. Hou, H.-H. Huang, D. Ghosh, J.-J. Shyue, L. Wang, S. Tretiak, X. Ma, W. Nie, Chem 2022, 8, 1107.
- [22] C. M. Perez, D. Ghosh, O. Prezhdo, W. Nie, S. Tretiak, A. Neukirch, J. Phys. Chem. Lett. 2022, 13, 5213.
- [23] S. Shrestha, H. Tsai, M. Yoho, D. Ghosh, F. Liu, Y. Lei, J. Tisdale, J. Baldwin, S. Xu, A. J. Neukirch, S. Tretiak, D. Vo, W. Nie, ACS Appl. Mater. Interfaces 2020, 12, 45533.
- [24] a) C. Zhao, W. Tian, Q. Sun, Z. Yin, J. Leng, S. Wang, J. Liu, K. Wu, S. Jin, J. Am. Chem. Soc. 2020, 142, 15091; b) X. Xiao, M. Wu, Z. Ni, S. Xu, S. Chen, J. Hu, P. N. Rudd, W. You, J. Huang, Adv. Mater. 2020, 32, 2004080.
- [25] L. Pan, Y. Feng, P. Kandlakunta, J. Huang, L. R. Cao, *IEEE Trans. Nucl. Sci.* 2020, 67, 443.